Biophotonics characterization of upconversion nanoparticles

by Lei DING

Thesis submitted in fulfilment of the requirements for the degree of

Doctor of Philosophy

under the supervision of Prof. Igor Aharonovich, Dr. Fan Wang

University of Technology Sydney
Faculty of Science

21/07/2022

Certificate of Original Authorship

I, Lei DING declare that this thesis is submitted in fulfilment of the requirements for the award of Doctor of Philosophy, in the School of Mathematical and Physical Sciences, Faculty of Science, at the University of Technology Sydney.

This thesis is wholly my own work unless otherwise reference or acknowledged. In addition, I certify that all information sources and literature used are indicated in the thesis.

This document has not been submitted for qualifications at any other academic institution.

This research is supported by the Australian Government Research Training Program and the China Scholarship Council Scholarship.

Signature:

Production Note:
Signature removed prior to publication.

Date: 21/07/2022

Acknowledgements

This thesis is the end of a long journey at UTS. It would not have been possible without the support and help from my family, supervisors, colleagues, and friends.

I would like to express my greatest gratitude to my supervisors. I thank **Prof. Igor Aharonovich** for timely help whenever I need it. I thank **Dr. Fan Wang** for offering me the extraordinary opportunity to work on optical technologies and for providing tremendous suggestions and guidance on my projects. I benefit a lot from your passion and dedication to research. I thank **Dr. Qiang Fu** for discussing the TTA project and for timely help whenever I need it. I thank **Prof. Dayong Jin** and **Pof. Jiajia Zhou** for their acceptance and supervision at the beginning of my PhD study.

I am grateful to all **Fan's Group members** that I have worked with during the past years. I particularly thank **Xuchen** for the great help with optical tweezers, Matlab, and Labview. I thank **Baolei** for teaching me optical knowledge and Matlab. I thank **Chaohao** for the help with super-resolution knowledge and experiments. I thank **Kevin** for keeping the Photonic Lab running and giving prompt assistance whenever it is required. I thank **Prof. David McGloin** and **Dr. Peter Reece** for their optical help.

I thank all the colleagues and friends in Photonic Lab and Faculty of Science: **Xiangjun** and **Dejiang** for the assistance in biological experiments and delicious food in daily life; **Ziqing**, **Shihui**, and **Xiaoxue** for the help with lanthanide-doped nanoparticles; **Ling**, for the happy chat during lunch; **Anna**, for discussion and instant help about optical tweezers; **Guochen**, for the chichat about life and fishing, and the help about organic synthesis in the first two years of my PhD study; **Guocheng**, for the car-service for relaxing at the weekend; **Mahnaz**, for the polymers for modifying nanoparticles and casual talk; **Peter (Qian)**, for the biological dishes; **Jiayan**, for the help about nanoparticles.

I thank my drinking buddies and basketball friends, **Dejiang**, **Chi**, **Milad**, **Xiaofei**, and **Mingshan**. I appreciate **Kang**, **Xuefei**, **Minghong** and **Feng** for the enjoyable time of talking and travelling.

Finally, I thank my family, **mother**, **father**, **sisters**, **aunt** and **uncles** for their continuous support and love throughout my whole life. I thank my girlfriend, **Hui**, for her understanding, care and support. I acknowledge the China Scholarship Council Scholarship for providing the scholarship.

Format of Thesis

This thesis is composed of six chapters. Chapter 1 is the introduction. Chapters 2-5 refer to the research results for the four goals (to see, sense, modulate, and develop new upconversion probes) in my PhD study. Chapter 6 gives the conclusion and perspective.

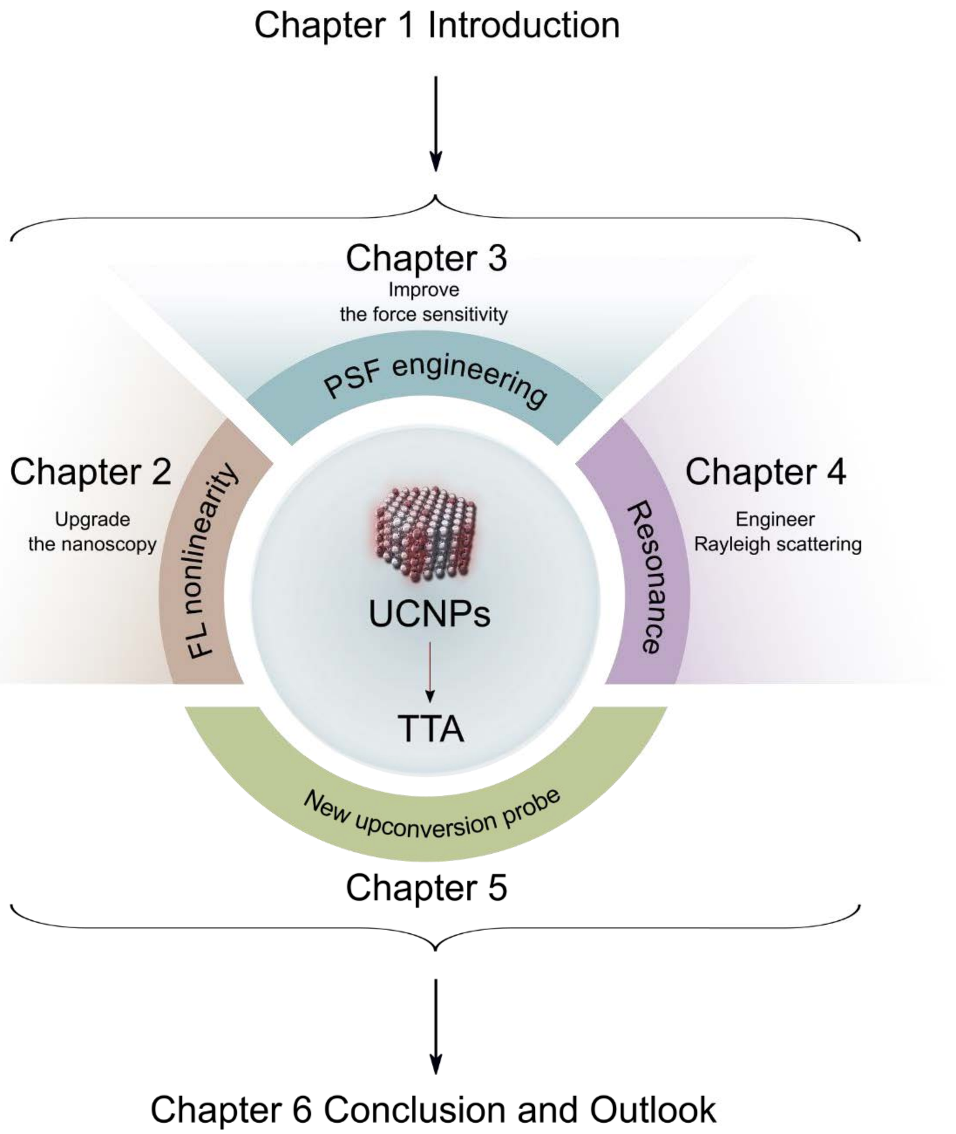

List of Publications

- Articles

1. **L. Ding**†, X. Shan†, P. Reece, I. Aharonovich and F. Wang*. Controlling Rayleigh scattering from lanthanide ion-doped nanoparticles. (*under review*)
2. X. Shan†, **L. Ding**† (co-first), S. Wen, J. Lu, J. Chennupati, X. Zhong*, D. Jin* and F. Wang*. Atto-Newton Force Sensitivity of Machine Learning Empowered Astigmatism Optical Tweezers. (*to be submitted*)
3. C. Chen†, **L. Ding**† (co-first), B. Liu and F. Wang*. Exploiting The Tunable Nonlinearity in Upconversion Nanoparticles for Super-resolution Imaging. (*under review*)
4. **L. Ding***, Q. Fu*, I. Aharonovich and F. Wang. Breaking Oxygen Quenching of Triplet–Triplet Annihilation Upconversion by Multidimensional Structures. (*to be submitted*)
5. **L. Ding**, J. Zhou*, Q. Fu, G. Bao, Y. Liu and D. Jin. Triplet-fusion Upconversion with Oxygen Resistance in Aqueous Media. Anal. Chem., 2021, 93, 4641–4646.
6. B. Liu, J. Liao, Y. Song, C. Chen, **L. Ding**, J. Lu, J. Zhou* and F. Wang*. Multiplexed Structured Illumination Super-Resolution Imaging with Lifetime-engineered Upconversion Nanoparticles. Nanoscale Adv., 2022.
7. X. Shan†, F. Wang†*, D. Wang, S. Wen, C. Chen, X. Di, P. Nie, J. Liao, Y. Liu, **L. Ding**, P. J. Reece* and D. Jin*. Optical Trapping Beyond Refractive Index Mismatch Using Highly Doped Nanoparticles. Nat. Nanotechnol., 2021, 1-7.
8. L. Zhang, K. Cook, A. Szmalenberg, B. Liu, **L. Ding**, F. Wang, D. McGloin*. Dual beam optical fiber traps for aerosols with angular deviation. Complex Light and Optical Forces XVI 12017, 2022, 126-132.

Table of Symbols

λ	laser wavelength	k_B	Boltzmann's constant
n	Refractive index	T	Temperature
σ_{sat}	Scattering cross-section	k	Stiffness
α	Polarizability	F_{ex}	Restoring force
ε	Permittivity	δ_{eq}	Position shift
φ	Phase difference	SD_{eq}	Standard deviation of position shift
I_r	Reflect light intensity	σ_k	Possibility variance of position
I_s	Scattering intensity	σ_p	Localisation accuracy
E_r	Reflect filed	ω	Angular frequency
E_s	Scattering field	k_m	Wavenumber
c_i	Energy transfer ratio	σ_i	Damping coefficient
k_{ij}	Cross-relaxation coefficient	ϕ_{UC}	UC quantum efficienc
a_{ij}	Branching ratio from energy level	η	Refraction coefficient
n_i	Population of photons	S_r	Sensitivity
w_i	Intrinsic decay rate	Q	Integral upconversion intensity
$F_i(x)$	Fluorescence intensities	$U(x)$	Potential energy
N_0	Fluorophore concentration	$g(x)$	Components of spatial information
k_B	Boltzmann's constant		

Abbreviations

UCNP	upconversion nanoparticle
HAADF-STEM	high-angle annular dark-field scanning transmission electron microscopy
Ln-NPs	lanthanide-doped nanoparticles
TEM	transmission electron microscopy
PSF	point spread function
TTA	triplet-triplet annihilation
ISC	intersystem crossing
NA	numerical aperture
STORM	stochastic optical reconstruction microscopy
PALM	photoactivated localisation microscopy
SIM	structured illumination microscopy
STED	stimulated emission depletion
SLM	spatial light modulator
QPD	quadrant photodiode detector
CCD	Charge-Coupled Device
CMOS	Complementary Metal Oxide Semiconductor
3D	three-dimensional
aN	attoNewton
iSCAT	interferometric scattering
SPAD	single-photon counting avalanche photodiode
FWHM	full width at half maximum
OA-VT	astigmatism video tracking
DNN	deep neural network

fN	femtoNewton
2D	two-dimensional
CL	cylindrical lens
PS	polystyrene sphere
M-iSCAT	multiplexed iSCAT
OA	oleic acid
ODE	1-octadecene
BF	bright-field
FL	fluorescence
PdTCPP	Pd(II) meso-Tetra(4-carboxyphenyl)porphine
QCDPA	5,5’-(9,10-anthracenediyl)diisophthalic acid
DMF	dimethyl formamide
NMR	nuclear magnetic resonance

Table of Contents

Certificate of Original Authorship ii

Acknowledgements i

Format of Thesis ii

List of Publications iii

Table of Symbols iv

Abbreviations v

Table of Contents vii

List of Figures x

List of Tables xvii

Abstract xviii

Chapter 1 Introduction 1

1.1 Fluorescent upconversion materials 1

1.1.1 Lanthanide-doped upconversion nanoparticles 2

1.1.2 Triple-fusion-based upconversion materials 5

1.2 Biophotonics technologies 6

1.2.1 Super-resolution microscopy 6

1.2.2 Optical tweezers 9

1.2.3 Interferometric scattering microscopy 11

1.3 Challenges to work out in the thesis 13

1.4 Organization of the thesis 14

Chapter 2 Upgrade the nanoscopy by leveraging the tunable fluorescence nonlinearity of UCNPs 16

2.1 Nonlinearity based super-resolution microscopy 16

2.2 Methods 18

2.2.1 Super-resolution microscopy system 18

2.2.2 Synthesis of UCNPs 19

2.3 Theory and simulation 19

2.3.1 Tunable fluorescent nonlinearity 19
2.3.2 Stepwise algorithm for UCNPs 23
2.3.3 Mechanism 23
2.3.4 Simulation 26
2.4 Resolution enhanced by stepwise 29
2.5 Conclusion 29
Chapter 3 Improve the force sensitivity of optical tweezers to aN level combining astigmatism and machine learning 31
3.1 Challenge of force sensing for current strategies 31
3.2 Methods 33
3.2.1 Optical astigmatism-enhanced optical tweezers 33
3.2.2 Deep neural network empowered optical astigmatism video tracking (DNN-OA-VT) .36
3.3 Results and discussion 39
3.3.1 3D trap by DNN-OA-VT 39
3.3.2 Force sensitivity analysis 40
3.3.3 aN-level force sensitivity simulation using Monte Carlo 43
3.4 Conclusion 47
Chapter 4 Engineer Rayleigh scattering of nanoparticles via doping lanthanide ions48
4.1 Limitation of engineering scattering for current strategies 48
4.2 Methods 51
4.2.1 Sample preparation 51
4.2.2 iSCAT microscopy 53
4.2.3 Multiplexed iSCAT (M-iSCAT) microscopy 53
4.3 Results and discussion 58
4.3.1 Simulation for ion resonance enhanced scattering 58
4.3.2 Scattering spectrum of lanthanide-doped nanoparticles 62
4.3.3 Multiplexed iSCAT microscopy for the identification of nanoparticles in living cells..64
4.4 Conclusion 67

Chapter 5 Break oxygen quenching of triplet-triplet annihilation upconversion in electrode medium **70**

5.1 Challenge of oxygen quenching for TTA 70

5.2 Methods 71

5.2.1 Synthesis of Pd(II) meso-Tetra(4-carboxyphenyl)porphine (PdTCPP) 71

5.2.2 Upconversion sample information 74

5.2.3 Spectral characterization 75

5.3 Results and discussion 76

5.3.1 TTA upconversion from organic solvent to water 76

5.3.2 TTA performance in air-saturated media 80

5.3.3 Potential in pH and temperature sensing 84

5.4 Conclusion 86

Chapter 6 Conclusion and Outlook **87**

6.1 Conclusion 87

6.2 Outlook 88

References **89**

List of Figures

Figure 1-1. UCNP and its properties. (**a**) Schematic of energy transfer for UCNP. (**b**) Transmission electron microscopy (TEM) images of $NaYF_4$ (upper) and high-angle annular dark-field scanning transmission electron microscopy (HAADF-STEM) image of 18-segment heterogeneous nanorods. Scale bar is 100 nm. (**c**) Luminescence micrograph of polystyrene beads tagged with $NaGdF_4$:Yb,Tm@$NaGdF_4$ (blue), $NaGdF_4$:Yb,Tm@$NaGdF_4$:Tb (green), $NaGdF_4$:Yb,Tm@$NaGdF_4$:Eu (red), and a binary mixture of $NaGdF_4$:Yb,Tm@$NaGdF_4$:Tb and $NaGdF_4$:Yb,Tm@$NaGdF_4$:Eu (yellow), respectively. Scale bar is 10 µm. (**d**) Power-dependent 800 nm-emission from a single UCNP with different Tm^{3+} doping concentration ($NaYF_4$:20% Yb^{3+}, x% Tm^{3+} nanoparticles, x=2, 3, 4, 6 and 8) under 980 nm excitation. Panels b, c and d adapted with permission from refs. [9], [10], [11] and [12], respectively; Copyright 2006 American Chemical Society; Copyright 2020 Springer Nature; Copyright 2011 Springer Nature; Copyright 2018 Springer Nature. 2

Figure 1-2. TTA and conventional TTA dyads. (**a**) Mechanism of energy transfer between sensitizer and annihilator. Superscript 3 denotes molecule with triplet, whole superscript 1 means molecule with singlet state. (**b**) Commonly used annihilators and sensitizers for a wide range of absorption and emission. Panel b adapted with permission from ref. [24]. Copyright 2021 Wiley-VCH. 5

Figure 1-3. Super-resolution mechanisms. (**a**) Rayleigh criterion for resolving ability. (b) Single-molecule localization mechanism. (**c**) Structured light mechanism. (**d**) PSF engineering for super-resolution microscopy. 7

Figure 1-4. Optical tweezers. (a) Schematic of laser potential wells in x and z directions and trapped particle. Upper and left are the potential energy along the distance. (b) Force balance of trapped particle in the potential well. (c) Typical setup of optical tweezers... 9

Figure 1-5. iSCAT microscopy. (a) Schematic of widefield illumination iSCAT (left) and rapid beam scanning illumination iSCAT (right). OBJ, objective; L1 and L2, lens; BS, beamsplitter; PBS, polarized beamsplitter; QWP, quarter-wave plate. (b) Schematic of the interference signal, *Ei* incident field, *Es* scattered field, *Er* reflected reference field, Δφ phase difference between the scattered and reflected fields. (c) Wide applications of iSCAT microscopy in protein imaging. Panels adapted with permission from refs. [51]

for a and b, and [52] for c; Copyright 2021 American Chemical Society; Copyright 2021 Springer Nature. 11

Figure 2-1. Setup of confocal microscopy used in this chapter. 18

Figure 2-2. Morphology and energy transfer. TEM (**a**) and simplified energy level and upconversion process (**b**) of the nanoparticles $NaYF_4$: 40% Yb^{3+}, 4% Tm^{3+} under 980 nm continuous-wave excitation. 20

Figure 2-3. The power-dependent curve (red dot) using the $NaYF_4$: 40% Yb^{3+}, 4% Tm^{3+} and 455 bandpass filter. The superlinear regime locates where the curve with the largest slope. Corresponding simulated full width at half maximum (FWHM) of single nanoparticle images at 455 nm emissions function of excitation intensity (cyan line). ..21

Figure 2-4. Extracting the higher-order nonlinear information. (a) Power-dependent curve of emission acquired under the gradient excitation powers. Dotted line represents the predicted emission according to the five-photon emission. (b) Comparison of super-linear and saturated emission distribution in the laser focus. (c) Extracting the nonlinear information provides a narrower PSF. 22

Figure 2-5. Schematic of the stepwise algorithm. (a) Scheme of the nonlinear power-dependent curve and three PSFs from raw images under three different excitation powers. (b) Sketch map of two-step (i), three-step (ii) and M-step (iii). 23

Figure 2-6. Simplified energy level diagram of Tm^{3+} and Yb^{3+} doped UCNP..........25

Figure 2-7. Simulation for resolving adjacent nanoparticles and X-bars. (a) Simulated fluorescent imaging (Grey) of two adjacent emitters with a distance from 160 nm to 210 nm under differential excitation intensity. Super-resolution imaging (Hot) results from two or three stepwise algorithms for comparison. FM represents the Fourier modulation process based on the results of 3-step. Scale bar is 200 nm. (b) The cross-section profiles of the simulated images of the nanoparticles with 160 nm distance in (a). (c-h) The simulation of the X-bar cross line shape structure with sparse UCNPs. Scale bars are 200 nm. 27

Figure 2-8. Resolving the signal UCNPs in sub-diffraction volume. (a) The 455 nm emission band image of UCNPs under a 980 nm excitation (0.1 mW, 0.2 mW, 0.3 mW) and their corresponding results with differential excitation multiple steps. (b) Line profiles of two nearby UCNPs from (a). Pixel dwell time, 1 ms. Pixel size, 20 nm. The scale bar is 200 nm. 29

Figure 3-1. Schematic of optical astigmatism-enhanced optical tweezers. 33

Figure 3-2. Measurement for lateral trap stiffness. (a) QPD method for measuring the lateral trap stiffness of 1 mm PS bead and 58 nm UCNP ($NaYF_4$,20%Yb,2%Er). *f*c is the corner frequency. (b) Comparison of signals from the QPD method and video tracking method. 34

Figure 3-3. Engineered PSF with astigmatism induced from cylindrical lens under different z position. (a) Lateral variations of PSF width of single trapped UCNP under different z positions. Insets are the images of the particle with astigmatism. (b) The x-y ratio of PSF width varying with the z position. (c) Location errors of the x-y ratio method. 35

Figure 3-4. Schematic diagram of astigmatism-empowered machine learning strategy. (**a**) The model obtained by recording the videos of the trapped nanoparticles under different z positions and recognising the features of PSF. (**b**) For z-position-unknown video, the trap stiffness can measure by position distribution fitting with Gaussian. 36

Figure 3-5. Position localisation accuracy. (a) Red line and dots represent the evaluation of predicted value and truth value. (b) 3D localisation accuracy of x-, y- and z-axis. The nanoparticle is NaYF4,20%Yb,2%Er, the diameter is 58nm. 38

Figure 3-6. Three-dimensional scatter plot of positions for a trapped nanoparticle. 39

Figure 3-7. Simulation of the optically trapped nanoparticle. (a) 3D positions plot for a single trapped nanoparticle and its projection. (b) 3D position distribution. laser power is 35.8mW, trap stiffnesses are 0.05, 0.137 and 0.026 pN/um/mW for x-, y- and z-axis, respectively. The scattering point is 1610. Data number Nr=1678.5, $SDeq$is 1.0859, 0.7429, and 1.6386 for x-, y- and z-axis, respectively. 43

Figure 3-8. The effect of force sensitivity on trap stiffness. (a) Scheme of the trapped nanoparticle moves under low and high stiffness. (b) Force sensitivity and position shift accuracy varying with trap stiffness. Assume $\sigma p$is 0. Data number Nr is 10000, laser power is from 10 to 90mW, stiffnesses are 0.05, 0.137 and 0.026 pN/um/mW for x-, y- and z-axis, respectively. 44

Figure 3-9. The effect of force sensitivity on data number. (a) Scheme of the trapped nanoparticle obtained with less and more points. (b) Force sensitivity varying with the data number for the x-, y- and z-axis. Assume $\sigma p$is 0. Laser power is 35.8 mW.......... 45

Figure 3-10. The effect of force sensitivity on localization accuracy. (a) Scheme of the trapped nanoparticle obtained with high and low accuracy. (b) Force sensitivity varying with localization accuracy for the x-, y- and z-axis. Laser power is 35.8 mW and the data number is 20000. 46

Figure 4-1. TEM images of the Yb-NCs (a), Er-NCs (b), Nd-NCs (c) and Tm-NCs (d). The scale bars are 100 nm. 51

Figure 4-2. (a) Sketch of the iSCAT microscopy system. (**b**) Schematics of iSCAT signal generation. 53

Figure 4-3. Schematic diagram of three-channel M-iSCAT microscopy. The objective lens (×60, NA=1.3, silicon oil) is used. 54

Figure 4-4. Calibration for M-iSCAT system using 1 µm polystyrene sphere. (a) The green-channel image. **(b)** The blue-channel image. **(c)** The iSCAT image. **(d)** The merge of green-channel, blue-channel and iSCAT channel. 55

Figure 4-5. Extracting scattering profile from iSCAT images. (a) The normalized detected signal of commercial polystyrene nanosphere with a low refractive index. **(b)** The selection of reference light to calculate the scattering spectrum under different illumination wavelengths. **(c)** The evaluation of scattering ratio (scattering to reference). **(d)** The scattering spectrum of polystyrene nanoparticles. Inset, the background-free images of polystyrene sphere under 940 nm (left) and 980 nm (right) where the background is measured by moving away nanoparticles. The scale bar in the figure is 1 µm. 56

Figure 4-6. Diagram of the resonance effect induced by lanthanide ions doped in nanoparticles under external illumination. 58

Figure 4-7. Energy level diagrams of Yb^{3+}, Er^{3+} and Nd^{3+} ions in $NaYF_4$ nanocrystal host, where ω is the dipole resonance angular frequencies. 59

Figure 4-8. Ytterbium, erbium and neodymium doping for enhancing the optical scattering. The numerical modeling of the real part **(i)** and imaginary part **(ii)** of the refractive index, and the scattering cross-section strength **(iii)** for SiO_2 sphere **(c)**, Yb^{3+} **(d)**, Er^{3+} **(e)**, and Nd^{3+} **(f)** doped nanoparticles. The nanoparticles in the simulation are treated as spheres with a radius of 25 nm. The concentration of resonator ions is set as 1.5 nm^{-3} for all three types of Ln-NCs. The surrounding media is air. 60

Figure 4-9. Comparison of iSCAT and FL images. (a) The bright-field (BF) image (merged with fluorescence image) of Yb-NCs and impurities. **(b)** The iSCAT images of Yb-NCs and impurities. (**c**) The corresponding fluorescence image (FL). The dotted rectangle points to impurities while the dotted circle represents Yb-NCs. The scale bars are 2 μm. **(d)** The fluorescence spectrum of Yb-NCs under the illumination wavelength of 980 nm. 62

Figure 4-10. Scattering spectrum of Ln-NCs. The scattering features of Yb-NCs (**a-i**), Er-NCs (**b-i**) and Nd-NCs (**c-i**), respectively. The square, circle and triangle with error bars represent the experiment data averaged from at least five measurements. The shadow lines suggest the simulated results. Typical iSCAT images of Ln-NCs under different excitation wavelengths are shown below the corresponding spectrum figure. The Yb-NCs, Er-NCs, and Nd-NCs are labelled by red, green, and blue dotted circles, respectively. The scale bars are 1μm. 63

Figure 4-11. Bright field of living HeLa cell (**a**) and the iSCAT image of the red rectangle region in the BF image of HeLa cell (**b**). The scale bars are 10 mm (a) and 2 mm (b), respectively. 64

Figure 4-12. (a) iSCAT image of HeLa cell. **(b-d)** M-iSCAT images of the orange square region at 3.4 **(b)**, 3.6 **(c)** and 4.5 **(d)** seconds, in which colorful circles represent different particles as labelled. The Ln-NCs (Er-1, Er-2 and Tm) can be distinguished from reference particles (Ref-1 and Ref-2) by merged fluorescence colors. The scale bars are 2 mm (a) and 1 mm (b-d) respectively. 65

Figure 4-13. Dependency of fluorescence and iSCAT trajectories of five particles within 2.5 seconds on horizontal (**a**) and vertical axises (**b**). 66

Figure 4-14. Dependency valuation of fluorescence and iSCAT trajectories via Fréchet distance, the radial distance of which is calculated considering both x and y positions. 67

Figure 5-1. [1]H NMR of (a) H_2TCPP and (b) PdTCPP. 73

Figure 5-2. TTA upconversion mechanism and TTA generation with oxygen resistance in aqueous media. (a) The energy level diagram showing the triplet fusion upconversion followed by the intersystem crossing (ISC) and triplet energy transfer (TET) processes in the pair of donor and acceptor. (b) The molecular structure of PdTCPP (donor) and QCDPA (acceptor). (c) The upconversion spectra of the TTA before (left) and after (right) adding base upon 532 nm laser excitation (52 mW cm^{-2}). Insets show the insoluble and soluble statues of the donor and acceptor molecules in water, and the snapshots behind the 532 nm short-pass edge filter (BSP01-532R-25, Semrock) under excitation of a 532 nm laser pen. D means donor, and A represents acceptor. (d) The spectra of TTA in DMF (left) and water (right), the concentrations of acceptor and donor are 5 mM and 0.1 mM, respectively. The excitation power density is 61 mW cm^{-2}. 76

Figure 5-3. (**a**) The upconversion intensity varying with the concentration of TTA-501 in water. The concentration of 1C means 0.1 mM for the donor and 5 mM for the acceptor. (**b**) The upconversion intensity varying with the concentration of TTA-501 in water. The concentration of 1C means 0.1 mM for the donor and 5 mM for the acceptor. (**c**) Upconversion emission intensity changes with the concentration of KOH. 77

Figure 5-4. Double log plot of the power-dependent emission intensity of the TTA systems with low (a), medium (b) and high (c) mole ratio of the donor and acceptor showing the slope change from quadratic to linear. 78

Figure 5-5. Double log plot of the power-dependent emission intensity of the samples in different media of 1 M KOH (a), 2 M KOH (b), TRIS (c) and PBS (d), respectively. .. 78

Figure 5-6. Upconversion efficiency under different excitation power densities. $Ru(bpy)_3Cl_2$ in water was used as a standard reference (absolute quantum efficiency Φ = 0.042 in aerated H_2O)[158]. The TTA-UC quantum efficiency (ΦUC) was calculated with the equation $\Phi UC = 2\Phi UC(ARef/A)(I/IRef)(\eta/\eta Ref)$, where A is the absorption at 532 nm, I is the emission intensity, η is the refraction of the medium. The multiplicative factor of 2 was reflected to represent the TTA mechanism (bimolecular process). 79

Figure 5-7. Influence of three kinds of electrolyte solutions on the upconversion emission with/without oxygen. 82

Figure 5-8. The durability of TTA in the solution of (a) water, (b) PBS buffer, (c) KH_2PO_4, (d) NaCl and (e) NH_4Cl with and without oxygen under 532 nm laser irradiation. 83

Figure 5-9. Aqueous TTA systems applied as pH sensors. (a) Reversibility of TTA as a pH sensor via adding HCl (1 M) and KOH (1 M) solution. (b) The decreased upconversion emission intensity evolution against the gradient adding of HCl (1 M). (c) The increasing trend of upconversion intensity via gradient adding of KOH (1 M). The error bars in a, b and c indicate the standard deviation of three measurements. The concentrations of acceptor and donor are 5 mM and 0.1 mM, respectively. The samples were tested under air-saturated conditions. The excitation power density is 61 mW cm^{-2}. Digital photos of TTA-501 (1M KOH) with HCl (d) and recovered state by KOH (e). 84

Figure 5-10. Aqueous TTA systems applied as temperature sensors. (d) Temperature-sensitive TTA upconversion in water (orange) and PBS (cyan) with inverse intensity evolution compared with traditional TTA systems. (e) The relative temperature sensing sensitivity calculated from data in (d) according to equation (5-6), $Sr = (\delta Q/\delta T)/Q$ (5-6). Q is the integral upconversion intensity. The error bars in a, b and c indicate the standard deviation of three measurements. The concentrations of acceptor and donor are 5 mM and 0.1 mM, respectively. The samples were tested under air-saturated conditions. The excitation power density is 61 mW cm^{-2}. 85

List of Tables

Table 2-1. Parameters in the internal transition. 25

Table 3-1. The parameters of four kinds of UCNPs ($NaYF_4$,20%Yb,2%Er) used for building DNN-OA-VT model. 36

Table 5-1. Feeding ratio of different aqueous/organic TTA samples. 74

Table 5-2. Aqueous TTA samples with different kinds of electrolytes. 75

Abstract

Upconversion materials have attracted enormous attention for a broad range of applications in biological imaging, energy-related light harvesting, and sensing, due to their unique physicochemical properties. However, the comprehensive understanding and characterization of upconversion nanoparticles for novel applications remain challenging. In this thesis, we set four goals to refresh the present characterization and provide a wider and deeper cognition of these upconversion nanoparticles. After the delicate design of optical setups and nanomaterials, we realized the super resolution enhancement, optical force sensitivity improvement, Rayleigh scattering modulation, and a new water-soluble molecular upconversion probe.

Experimentally and theoretically, we upgrade the nanoscopy by exploiting the unique nonlinearity of upconversion nanoparticles using conventional confocal microscopy. We realize three-dimensional attoNewton-level optical force of optical via revolutionizing the configuration, data collection and accuracy analysis based on the property of upconversion nanoparticles. We refresh the morphology-independent method of engineering Rayleigh scattering at the nanoscale level based on the resonance effect of upconversion nanoparticles. We develop water-soluble molecular upconversion materials based on the ionic equilibrium of upconversion dyes. Based on the improved characterization of upconversion materials, as well as the technologies, we anticipate the potential applications in future, such as, deep tissue imaging, monitoring the interaction in the limit region (e.g., attoNewton level), and multiplexed scattering microscopy of cell dynamics.